

# YOLO-DS: Fine-Grained Feature Decoupling via Dual-Statistic Synergy Operator for Object Detection

Lin Huang<sup>a,g,h</sup>, Yujuan Tan<sup>b,\*</sup>, Weisheng Li<sup>c</sup>, Shitai Shan<sup>g,h</sup>, Liu Liu<sup>d</sup>, Bo Liu<sup>e</sup>, Linlin Shen<sup>f</sup>, Jing Yu<sup>a</sup>, Yue Niu<sup>a</sup>

<sup>a</sup>*Chongqing University, No.55, University Town South Road, Gaoxin District, Chongqing, 401331, China*

<sup>b</sup>*National University of Defense Technology, No.1, Fuyuan Road, Kaifu District, Changsha, 410073, China*

<sup>c</sup>*Chongqing University of Posts and Telecommunications, No.2, Chongwen Road, Nan'an District, Chongqing, 400065, China*

<sup>d</sup>*China Academy of Information and Communications Technology, No.52, Huayuan North Road, Haidian District, Beijing, 100191, China*

<sup>e</sup>*Fawer Automotive Components Co., Ltd, No.777, Dongfeng South Street, Changchun Automobile Economic and Technological Development Zone, Changchun, 130062, China*

<sup>f</sup>*Shenzhen University, No.3688 Nanshan Avenue, Nanshan District, Shenzhen, 518061, China*

<sup>g</sup>*Inspur Yunzhou Industrial Internet Co., Ltd, No.1036 Langchao Road, Lixia District, Jinan, Shandong, 250101, China*

<sup>h</sup>*Guoqi Zhimo (Chongqing) Technology Co., Ltd., 5th Floor, Building B15, Xiantao Data Valley, Yubei District, Chongqing, 401122, China*

---

## Abstract

One-stage object detection, particularly the YOLO series, strikes a favorable balance between accuracy and efficiency. However, existing YOLO detectors lack explicit modeling of heterogeneous object responses within shared feature channels, which limits further performance gains. To address this, we propose YOLO-DS, a framework built around a novel Dual-Statistic

---

\*Corresponding Author

Email addresses: h72001346@163.com (Lin Huang), tanyujuan@nudt.edu.cn (Yujuan Tan ), liws@cqupt.edu.cn (Weisheng Li), shansht@inspur.com (Shitai Shan), 244319450@qq.com (Liu Liu), liubo@fawer.com.cn (Bo Liu), llshen@szu.edu.cn (Linlin Shen), 20201401010@cqu.edu.cn (Jing Yu), yuen@cqu.edu.cn (Yue Niu)

Synergy Operator (DSO). The DSO decouples object features by jointly modeling the channel-wise mean and the peak-to-mean difference. Building upon the DSO, we design two lightweight gating modules: the Dual-Statistic Synergy Gating (DSG) module for adaptive channel-wise feature selection, and the Multi-Path Segmented Gating (MSG) module for depth-wise feature weighting. On the MS-COCO benchmark, YOLO-DS consistently outperforms YOLOv8 across five model scales (N, S, M, L, X), achieving AP gains of 1.1% to 1.7% with only a minimal increase in inference latency. Extensive visualization, ablation, and comparative studies validate the effectiveness of our approach, demonstrating its superior capability in discriminating heterogeneous objects with high efficiency.

*Keywords:*

YOLO, Object Detection, Dual-Statistic Synergy Operator, Fine-Grained Feature Decoupling, Gating Mechanism

---

## 1. Introduction

One-stage object detection[1, 2, 3, 4, 5, 6, 7, 8, 9, 10, 11, 12, 13, 14, 15, 16, 17, 18, 19, 20, 21, 22, 23] frameworks, especially the YOLO series, are renowned for their optimal trade-off between accuracy and speed, enabling widespread real-time applications. Nonetheless, a fundamental limitation persists: these detectors operate on a shared channel modeling scheme, failing to explicitly distinguish the distinct response patterns of heterogeneous objects (e.g., small vs. large, foreground vs. background). This homogenized representation triggers channel-wise competition and impedes dynamic attention allocation, ultimately capping detection performance.

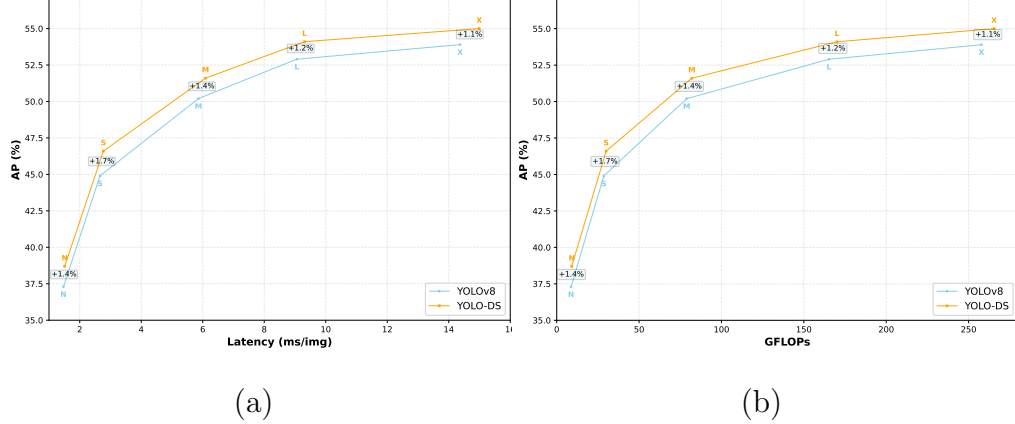


Figure 1: Comparison of the proposed YOLO-DS with YOLOv8.

While attention mechanisms like SENet[24] and CBAM[25] attempt to recalibrate features, they exhibit critical shortcomings for this task. SENet relies exclusively on global mean statistics for channel recalibration, which inadequately represents heterogeneous activation patterns induced by diverse object scales. Building upon SENet, CBAM further introduces spatial attention by exploiting both spatial average and max statistics, yet its global spatial aggregation inevitably mixes activation responses from multiple objects, thereby obscuring fine-grained channel semantics. Although multi-head self-attention (MHSA) in ViT[26] models global dependencies via multiple attention heads, feature interactions within each head remain implicitly entangled, where responses from small or sparse objects are prone to being overwhelmed. Moreover, pursuing finer-grained head-wise decomposition leads to a quadratic increase in computational cost, making it less suitable for real-time detection.

To bridge this gap, we propose YOLO-DS. Our core contribution is the **Dual-Statistic Synergy Operator (DSO)**, which explicitly models the

channel-wise mean ( $\mu$ , representing overall strength) and the peak-to-mean difference ( $d$ , representing sparsity/saliency) in a synergistic 2D decision space[27]. This allows for the natural decoupling of feature responses into categories such as small objects, large objects, mixed-scale objects and background. Leveraging the DSO, we further introduce:

1. The **Dual-Statistic Synergy Gating (DSG)** Module: A channel gating mechanism that uses DSO outputs to generate adaptive weights, enhancing discriminative features and suppressing noise.
2. The **Multi-Path Segmented Gating (MSG)** Module: A depth-wise gating mechanism that dynamically weights features from different network depths within the C2F structure, optimizing representations for objects of varying scales.

Integrated into the YOLO architecture, YOLO-DS delivers consistent and scalable improvements. On MS-COCO[28], it outperforms YOLOv8[12] across all model scales (N, S, M, L, X) by 1.1–1.7% AP[28] (Fig.1) with negligible latency overhead.

## 2. Methodology

### 2.1. *Dual-Statistic Synergy Operator (DSO)*

We first conduct a systematic analysis of the limitations of SENet, CBAM, and multi-head self-attention mechanisms[26] in modeling heterogeneous objects. Further statistical analysis of channel response distributions reveals that neither the channel-wise mean nor the maximum activation alone is sufficient to distinguish different object types. To this end, we adopt the channel-wise mean ( $\mu$ ) and the peak-to-mean difference ( $d$ ) as two comple-

mentary statistical descriptors for characterizing channel responses. Specifically, the channel-wise mean reflects the overall activation strength, while the peak-to-mean difference captures the degree of response sparsity, highlighting the discrepancy between localized strong activations and globally weak responses. By jointly modeling these two statistics, object representations can be categorized into four canonical patterns: small objects, large objects, mixed-scale objects, and background (no-object) responses. Assuming the input feature map is  $x \in \mathbb{R}^{B \times C \times H \times W}$ . The detailed computation is given as follows:

$$\mu_{b,c} = \frac{1}{HW} \sum_{h=1}^H \sum_{w=1}^W x_{b,c,h,w}, \quad \mu \in \mathbb{R}^{B \times C \times 1 \times 1} \quad (1)$$

$$m_{b,c} = \max_{h,w} x_{b,c,h,w}, \quad m \in \mathbb{R}^{B \times C \times 1 \times 1} \quad (2)$$

$$d_{b,c} = m_{b,c} - \mu_{b,c}, \quad d \in \mathbb{R}^{B \times C \times 1 \times 1} \quad (3)$$

where  $\mu_{b,c}$  and  $m_{b,c}$  denote the channel-wise mean and maximum response, respectively, and  $d_{b,c}$  represents the peak-to-mean difference. Rather than treating the two statistics independently, we aim to explicitly model the coupled effects of the channel-wise mean and the peak-to-mean difference within a two-dimensional decision space:

$$s_{b,c} = (\mu_{b,c}, d_{b,c}) \in \mathbb{R}^2 \quad (4)$$

where  $\mu_{b,c}$  characterizes the overall activation strength, and  $d_{b,c}$  reflects the degree of response sparsity and localized saliency. To capture the coupled relationship between overall activation strength ( $\mu$ ) and response sparsity ( $d$ ), we design the DSO as a synergistic function:

$$\Phi(\mu, d) = (d + 1)(\mu + 1) - 1 \quad (5)$$

which can be equivalently expanded as

$$\Phi(\mu, d) = \mu d + \mu + d \quad (6)$$

$$y_{b,c} = \Phi(\mu_{b,c}, d_{b,c}), \quad y \in \mathbb{R}^{B \times C \times 1 \times 1} \quad (7)$$

where  $y_{b,c}$  denote the channel-wise decision response produced by our DSO. To gain deeper insight into the DSO, we compute the partial derivatives of Eq.6 as follows:

$$\frac{\partial \Phi}{\partial \mu} = d + 1 > 0, \quad \frac{\partial \Phi}{\partial d} = \mu + 1 > 0 \quad (8)$$

Therefore, under the constraint of non-negative feature activations the DSO  $\Phi(\mu, d)$  is strictly monotonically increasing with respect to both  $\mu$  and  $d$ . This indicates that stronger global activation (an increase in  $\mu$ ) or greater local sparsity (an increase in  $d$ ) will both lead to an increase in the value of  $\Phi$ . Further compute the second-order partial derivatives:

$$\frac{\partial}{\partial d} \left( \frac{\partial \Phi}{\partial \mu} \right) = \frac{\partial}{\partial d} (d + 1) = 1 > 0, \quad \frac{\partial}{\partial \mu} \left( \frac{\partial \Phi}{\partial d} \right) = \frac{\partial}{\partial \mu} (\mu + 1) = 1 > 0 \quad (9)$$

Based on the analysis of Eq.9, it can be observed that a larger value of  $d$  enhances the marginal contribution of  $\mu$  to  $\Phi$ , while a larger  $\mu$  similarly increases the marginal contribution of  $d$  to  $\Phi$ . This indicates a synergistic relationship between  $\mu$  and  $d$ , where each variable reinforces the contribution of the other to the overall response  $\Phi$ .

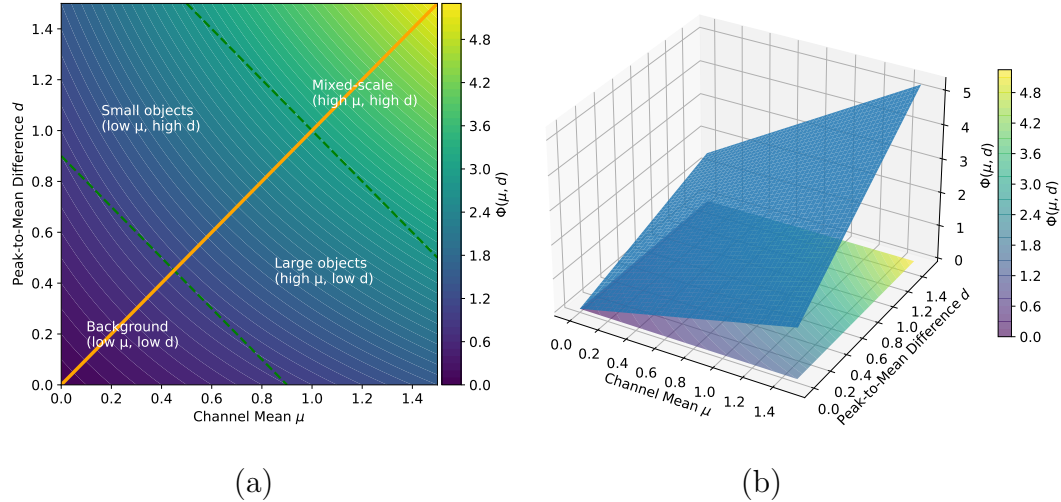


Figure 2: (a) Two-dimensional contour map of the DSO response as a function of  $\mu$  and  $d$ . (b) Three-dimensional rendering of  $\Phi(\mu, d)$ , explicitly showing the nonlinear surface shaped by the interplay of activation strength and sparsity.

To gain deeper insight into the behavior of the proposed DSO, we visualize its response in both two-dimensional and three-dimensional forms, as shown in Fig.2 (a) and Fig.2 (b), respectively. The orange solid line in Fig.2 (a), given by  $d = \mu$  (corresponding to  $m = 2\mu$ ), provides an effective boundary that partitions the response region. As this orange boundary extends toward positive infinity in both  $d$  and  $\mu$ , the corresponding activation strength increases strictly monotonically. Therefore, the region above this orange line (i.e.,  $d > \mu, m > 2\mu$ ) can be defined as the sparse-salient (or locally focused) region, where the maximum activation exceeds the mean. This indicates that only a small number of spatial locations in the feature map—such as keypoints of objects or centers of small objects—are strongly activated, while most areas exhibit weak responses. The activation distribution is highly

non-uniform and sparse. This region typically corresponds to salient local features such as small objects, edges, and fine texture details. Conversely, the region below the orange line (i.e.,  $d < \mu, m < 2\mu$ ) can be defined as the uniform-broad (or globally diffuse) region, where the difference between the maximum activation and the mean is relatively small. This implies that activations are distributed more evenly and extensively across spatial locations, without sharp peaks, and all positions contribute relatively uniformly to the response. This region generally corresponds to large objects, background, or broadly distributed features with low contrast.

To clearly distinguish between different objects, we introduce two non-deterministic boundaries (green dashed lines in Fig.2 (a)) to partition all responses  $\Phi$  into four fuzzy regions, which are used to differentiate small objects, large objects, mixed-scale objects, and background. These four regions are specifically defined as follows:

- Small Objects: Characterized by a high value of  $d$  and a relatively low value of  $\mu$ , satisfying  $d > \mu, m > 2\mu$ . This corresponds to the upper-left region in Fig.2 (a).
- Large Objects: Characterized by a high value of  $\mu$  and a relatively low value of  $d$ , satisfying  $d < \mu, m < 2\mu$ . This corresponds to the lower-right region in Fig.2 (a).
- Mixed-Scale Objects: Exhibit both locally strong responses and broadly weak responses, with both statistical measures  $\mu$  and  $d$  taking relatively high values. These objects fluctuate approximately along the direction where  $d \approx \mu$ , in regions where  $\Phi$  shows stronger responses, correspond-

ing to the upper-right area in Fig.2 (a).

- Background: Both  $\mu$  and  $d$  are low, fluctuating approximately along the direction where  $d \approx \mu$ , in regions where  $\Phi$  shows weaker responses, corresponding to the lower-left area in Fig.2 (a).

Except for one decision boundary ( $d = \mu, m = 2\mu$ , orange solid line in Fig.2 (a)) which is fixed, the four fuzzy regions determined by the two non-deterministic boundaries (green dashed lines in Fig.2 (a)) we introduce are not rigid. They primarily serve as a visual schematic for analysis. In practice, their precise delineation must be further refined by learning the feature distribution from input samples. Furthermore, among these four categories, all except the background are susceptible to varying degrees of noise interference. For example, the small-object category may be perturbed by sparse, high-response noise points, while the large-object category could be affected by extensive background noise. Consequently, filtering via learning from diverse sample features remains essential.

In summary, the proposed DSO acts as a feature decoupling mechanism for different objects and a preprocessing step for object classification before the gating network learns the features. By doing so, it enables the gating network to better learn the distinctive features of different objects, thereby facilitating more effective classification. In an adaptive manner, it dynamically retains highly activated features while discarding redundant ones, ultimately enhancing the detection accuracy (AP) of the object detection network.

## 2.2. Dual-Statistic Synergy Gating (DSG)

Although the DSO decouples features of different objects and serves as a preprocessing step for object classification, the derived features remain susceptible to two types of interference: cross-category feature mixing and contamination by noise. To address these issues, we introduce a  $1 \times 1$  convolutional layer after DSO. This trainable convolution further purifies the feature representations by enhancing discriminative signals and suppressing both inter-class interference and noise within the pre-classified groups. Subsequently, a sigmoid function activates the refined feature maps. Features are then gated by the resulting 0–1 weights, where redundant or noisy activations are suppressed, and informative ones are selected to implement an attentional gating mechanism. We term this module the Dual-Statistic Synergy Gating (DSG) network (the blue region in Fig.3). Its main computational procedure is as follows:

$$\begin{aligned} z_{DSG} &= \mathbf{W}_{DSG} * y + \mathbf{b}_{DSG}, \quad z_{DSG} \in \mathbb{R}^{B \times C' \times 1 \times 1}, \\ \mathbf{W}_{DSG} &\in \mathbb{R}^{C' \times C \times 1 \times 1}, \mathbf{b}_{DSG} \in \mathbb{R}^{C'}, C' = \lfloor \frac{C}{2} \rfloor \times (2 + n) \end{aligned} \quad (10)$$

$$w_{DSG} = \sigma(z_{DSG}) = \frac{1}{1 + e^{-z_{DSG}}}, \quad w_{DSG} \in \mathbb{R}^{B \times C' \times 1 \times 1} \quad (11)$$

$$x_{out} = w_{DSG} \odot x_{cat}, \quad x_{out} \in \mathbb{R}^{B \times C' \times H \times W}, x_{cat} \in \mathbb{R}^{B \times C' \times H \times W} \quad (12)$$

where  $\mathbf{W}_{DSG}$  represents the  $1 \times 1$  convolutional kernel transforming  $C$  input channels to  $C'$  output channels,  $\mathbf{b}_{DSG}$  is the bias vector of dimension  $C'$ ,  $n$  denotes the number of bottleneck blocks[29],  $\sigma$  is the sigmoid activation function,  $x_{cat}$  corresponds to the feature concatenation point in the C2F structure[12], and  $x_{out}$  is the final output.

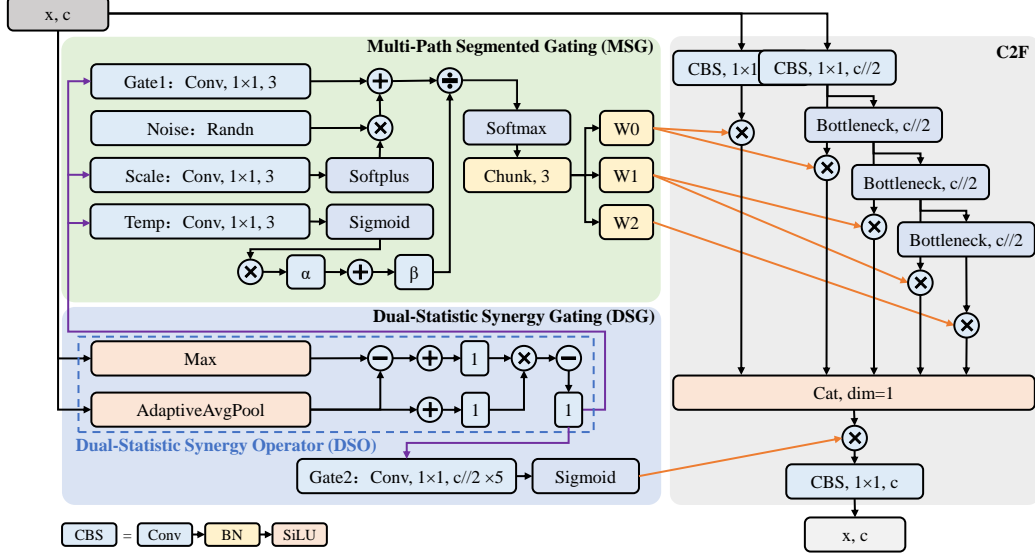


Figure 3: Structural diagram of the C2F architecture incorporating the DSG and MSG modules.

Overall, this gating module serves as a complementary addition to the DSO. It effectively decouples heterogeneous object features through the synergistic interaction of the dual statistics ( $d$  and  $\mu$ ) across different input samples. Furthermore, in a learnable manner, it further filters cross-category features and interference noise, adaptively forming more discriminative heterogeneous object representations, which in turn produce effective gating weights. These weights efficiently regulate the multi-channel features at the information-intensive concatenation point in the C2F structure, preserving informative features while suppressing redundant ones. This mechanism successfully decouples the features of small objects, large objects, mixed-scale, and background, leading to significant gains in AP with minimal computational overhead.

### 2.3. Multi-Path Segmented Gating (MSG)

In the C2F module, multiple bottleneck blocks are stacked sequentially, and their intermediate outputs are concatenated. Although these features share the same spatial resolution, their corresponding effective network depths differ due to varying computational path lengths. Consequently, features from different concatenation paths exhibit distinct representational biases in terms of semantic abstraction and receptive field. It has been shown that early bottleneck outputs preserve fine-grained spatial details and local structures, which facilitates feature extraction for small objects, whereas deeper bottleneck outputs encode more abstract semantic and contextual information, making them more suitable for large-object feature extraction and background suppression[30, 31, 32]. Therefore, treating all bottleneck outputs equally leads to suboptimal feature utilization.

Although the proposed DSO and DSG modules effectively discriminate heterogeneous objects, the relative importance of different network depths in extracting discriminative features for heterogeneous objects has not yet been sufficiently explored, which limits further improvements in detection performance. To address this issue, we further group different computational paths within the C2F structure according to their effective network depths, and employ a softmax-based weighting strategy to balance the contributions of different groups. This design enables an adaptive competition among depth-level features, allowing objects of different scales to dynamically select suitable representations from shallow to deep network layers. Moreover, to enhance the robustness of the grouping weights, we introduce an adaptively scaled Gaussian-distributed random noise, together with an

adaptive multi-dimensional temperature control module that flexibly regulates the sharpness of the weight distribution. The resulting module is termed Multi-Path Segmented Gating (MSG), as illustrated by the green region in Fig.3. The detailed computational procedure of MSG is described as follows:

$$z_{MSG} = \mathbf{W}_{MSG} * y + \mathbf{b}_{MSG}, \quad z_{MSG} \in \mathbb{R}^{B \times 3 \times 1 \times 1}, \quad (13)$$

$$\mathbf{W}_{MSG} \in \mathbb{R}^{3 \times C \times 1 \times 1}, \mathbf{b}_{MSG} \in \mathbb{R}^3$$

$$z_{scale} = \mathbf{W}_{scale} * y + \mathbf{b}_{scale}, \quad z_{scale} \in \mathbb{R}^{B \times 3 \times 1 \times 1}, \quad (14)$$

$$\mathbf{W}_{scale} \in \mathbb{R}^{3 \times C \times 1 \times 1}, \mathbf{b}_{scale} \in \mathbb{R}^3$$

$$z_{noise} = \ln(1 + e^{z_{scale}}) \odot \epsilon, \quad \epsilon \sim \mathcal{N}(0, I), \epsilon \in \mathbb{R}^{B \times 3 \times 1 \times 1} \quad (15)$$

$$\mathcal{T} = \alpha \cdot \sigma(\mathbf{W}_t * y + \mathbf{b}_t) + \beta = \alpha \cdot \frac{1}{1 + e^{-(\mathbf{W}_t * y + \mathbf{b}_t)}} + \beta, \quad (16)$$

$$\mathcal{T} \in \mathbb{R}^{B \times 3 \times 1 \times 1}, \mathbf{W}_t \in \mathbb{R}^{3 \times C \times 1 \times 1}, \mathbf{b}_t \in \mathbb{R}^3$$

$$w_{MSG} = \text{Softmax}\left(\frac{z_{MSG} + z_{scale}}{\mathcal{T}}\right), \quad w_{MSG} \in \mathbb{R}^{B \times 3 \times 1 \times 1} \quad (17)$$

where  $\mathbf{W}_{MSG}$  and  $\mathbf{b}_{MSG}$  denote the weight and bias of the  $1 \times 1$  convolution in the gating component, respectively. The weights are divided into three groups, the rationale for which will be detailed in the experimental section. The resulting gating signal is denoted as  $z_{MSG}$ . For the adaptive noise scaling pathway,  $\mathbf{W}_{scale}$  and  $\mathbf{b}_{scale}$  represent the convolutional weight and bias, yielding the scaling factor  $z_{scale}$ . A Gaussian-distributed random noise  $\epsilon$  is then modulated by  $z_{scale}$  to produce the adaptive random noise  $z_{noise}$ . In the adaptive multi-dimensional temperature control module,  $\mathbf{W}_t$  and  $\mathbf{b}_t$  correspond to the weight and bias of another  $1 \times 1$  convolution. The module employs two fixed scaling parameters,  $\alpha$  and  $\beta$ , which are set to 1.9 and 0.1 respectively, as this configuration was found to yield the best performance in

our experiments. The output of this module is denoted as the adaptive multi-dimensional temperature term  $\mathcal{T}$ . Finally, the grouped weighting coefficients  $\mathbf{W}_{MSG}$  are obtained by normalizing the combined gating and temperature-adjusted signals through a softmax operation.

Overall, the MSG module groups features of varying network depths within the C2F structure before their concatenation and adaptively modulates the weights assigned to different depth levels. This design enables a further, effective optimization of feature contributions for both large and small objects from the perspective of network depth. Consequently, it enhances AP with only minimal computational overhead. This approach provides a complementary enhancement to the DSO and DSG modules in distinguishing heterogeneous objects by introducing an adaptive gating mechanism along the depth dimension.

### 3. Experiments

To evaluate model performance, all experiments were conducted on a workstation equipped with eight NVIDIA GeForce RTX 4090 GPUs. Training was performed using the MS COCO 2017 dataset[28], which comprises approximately 118,287 training images and 5,000 validation images across 80 object categories, serving as a common benchmark for object detection algorithms. For comparative experiments, the baseline models were selected from the widely adopted YOLOv8 series (including the n, s, m, l, and x variants), while the improved models were from the YOLO-DS series (also including the n, s, m, l, and x variants). To ensure a fair comparison, all models were trained from scratch using the official codebases and recommended hyper-

parameters until convergence, with a consistent input resolution of  $640 \times 640$  pixels and the same data augmentation strategies. Evaluation metrics followed the common practice in object detection, including mean Average Precision (AP)—specifically AP@50-95 (averaged over IoU thresholds from 0.5 to 0.95)—along with the number of parameters, FLOPs, and inference speed (latency) measured on a T4 GPU with TensorRT acceleration.

### *3.1. Visualization Analysis*

To further investigate the effectiveness of the proposed YOLO-DS, we employ Eigen-CAM[33] to visualize the attention distributions of different detectors. Eigen-CAM provides an intuitive interpretation of how models allocate spatial attention across feature maps, enabling a qualitative comparison of feature utilization and target perception capability under various object scale and density conditions.

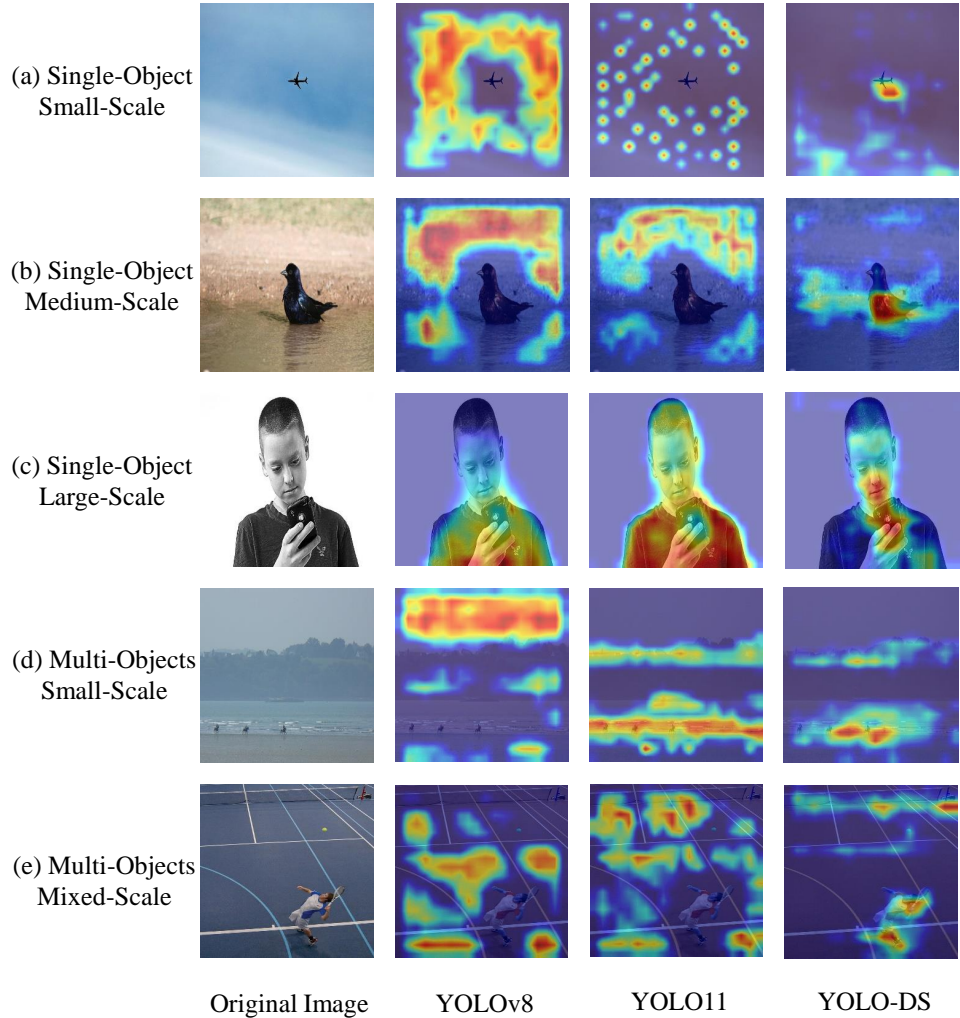


Figure 4: Eigen-CAM visualization of attention responses for different object-scale and object-density scenarios.

As illustrated in Fig.4, YOLOv8 and YOLO11[15] fail to explicitly differentiate objects of varying scales, which leads to noticeable attention misalignment in small-object detection scenarios (Fig.4(a), (b), (d), and (e)). Specifically, a considerable portion of the activation responses is distributed

over background regions rather than being concentrated on target objects. Although YOLO11 incorporates multi-head self-attention, the limited number of attention heads inevitably causes responses from small objects to be overwhelmed by large objects or background features, resulting in suboptimal performance on small-object detection. In contrast, YOLO-DS consistently produces more compact and discriminative activation maps across all scenarios. For single small-scale objects, the proposed method generates sharp and highly localized activation peaks, indicating its ability to amplify sparse yet salient responses.

For large-scale objects, an important observation is that YOLO-DS does not simply maximize attention over the entire object extent (Fig.4(c)). Compared with YOLOv8 and YOLO11, whose responses tend to uniformly cover large objects, YOLO-DS yields more selective activations that emphasize discriminative local structures and fine-grained details, such as object boundaries and semantically informative regions. This behavior is consistent with the design of our DSO. When the channel-wise mean activation is high, uniformly strong responses often indicate feature redundancy or limited discriminative power. By jointly considering the peak-to-mean difference and the mean activation, YOLO-DS suppresses excessive homogeneous responses and reallocates attention to locally salient regions. Consequently, the model focuses on critical fine-grained details rather than indiscriminately amplifying the entire object region.

Overall, YOLO-DS demonstrates a scale-adaptive attention behavior: it amplifies sparse peaks for small objects while prioritizing discriminative details over redundant regions for large objects.

### 3.2. Ablation Experiment

To validate the effectiveness of the DSG and MSG modules, we conducted a systematic ablation study by successively integrating each module into the baseline model for performance evaluation. Furthermore, to determine the number of groups in the MSG module as well as the values of parameters  $\alpha$  and  $\beta$ , a series of experiments were carried out by varying the group count and adjusting  $\alpha$  and  $\beta$ . The final parameter configuration was established based on the optimal experimental results.

Table 1: Ablation Study on MSG Performance under Varying Group Counts ( $\alpha = 1, \beta = 0$ ).

Group Count	AP(%)	Params(M)	GFLOPs
Baseline	52.9	43.7	165.2
2	52.9( <span style="color:red">0.0</span> )	43.8	165.8
3	53.3( <span style="color:green">+0.4</span> )	43.8	165.8
4	53.1( <span style="color:red">+0.2</span> )	43.8	165.8
FullPath	53.0( <span style="color:red">+0.1</span> )	43.8	165.8

First, we conduct an ablation study on the grouping strategy of the MSG module. Experiments are carried out by varying the number of groups from 2 to 4, as well as applying no grouping—where weights are assigned individually to each path. As shown in Tab.1, the experimental results indicate that the three-group configuration achieves the best performance, with an AP improvement of 0.4%. Therefore, we fix the number of groups to three and apply distinct weighting mechanisms to features from different network

depths.

Table 2: Ablation Study on MSG Performance with Different  $\alpha$  Values ( $\beta = 0.1$ ,  $GroupCounts = 3$ ).

$\alpha$	AP(%)	Params(M)	GFLOPs
Baseline	52.9	43.7	165.2
0.9	53.2(+0.3)	43.8	165.8
1.9	53.6(+0.7)	43.8	165.8
2.9	53.3(+0.4)	43.8	165.8
3.9	53.0(+0.1)	43.8	165.8
4.9	53.1(+0.2)	43.8	165.8

We further conduct an ablation study on the parameters  $\alpha$  and  $\beta$  in the multi-dimensional temperature control module of MSG. Since the optimal grouping configuration was determined to be three groups in prior experiments, all trials in this section are performed under the condition of  $GroupCounts = 3$ . The value of  $\beta$  is kept constant at 0.1, while  $\alpha$  is varied across a predefined range. As shown in Tab.2, the model achieves the best performance when  $\alpha$  is set to 1.9, surpassing the baseline by 0.7% in AP. Accordingly,  $\alpha = 1.9$  is selected as the fixed parameter for all subsequent experiments.

Additionally, to validate the effectiveness of our proposed DSO, we replace it with an adaptive mean pooling operator (Mean) and a channel-wise maximum operator (Max) within the DSG and MSG modules, respectively, and conduct corresponding ablation studies.

Table 3: Ablation Study on DSG Performance with Different Operators (Max, Mean, and DSO).

<i>Operator</i>	AP(%)	Params(M)	GFLOPs
Baseline	52.9	43.7	165.2
Mean	53.1( <b>+0.3</b> )	49.8	170.1
Max	52.7( <b>-0.2</b> )	49.8	170.1
DSO	53.5( <b>+0.6</b> )	49.8	170.1

As shown in Tab.3, after integrating the DSG module into the Baseline, the model achieves the best performance when the DSO is used within DSG, yielding an AP improvement of 0.5%. Therefore, in the DSG module, DSO significantly outperforms both the adaptive mean pooling operator and the channel-wise maximum operator.

Table 4: Ablation Study on MSG Performance with Different Operators (Max, Mean, and DSO).

<i>Operator</i>	AP(%)	Params(M)	GFLOPs
Baseline	52.9	43.7	165.2
Mean	53.5( <b>+0.6</b> )	43.8	165.8
Max	52.9( <b>0.0</b> )	43.8	165.8
DSO	53.6( <b>+0.7</b> )	43.8	165.8

As shown in Tab.4, when the MSG module is individually incorporated into the baseline, the model attains its optimal performance by employing the DSO within MSG, which yields an AP improvement of 0.7%. Hence,

in the MSG module, DSO demonstrates substantially superior performance compared to both the adaptive mean pooling operator and the channel-wise maximum operator.

Table 5: Ablation Study on DSG and MSG Modules.

Baseline	DSG	MSG	AP(%)	Params(M)	GFLOPs
✓	-	-	52.9	43.7	165.7
✓	✓	-	53.5 ( <b>+0.6</b> )	49.8	170.1
✓	-	✓	53.6 ( <b>+0.7</b> )	43.8	165.8
✓	✓	✓	54.1 ( <b>+1.2</b> )	49.8	170.1

Finally, we conduct an ablation study by integrating the finalized DSG and MSG modules—each with its determined parameters and operators—into the baseline, both individually and jointly. As shown in Tab.5, incorporating the DSG module alone yields an AP gain of 0.5%, while adding the MSG module alone leads to an improvement of 0.7% in AP. When both modules are combined, the model achieves a notable AP increase of 1.2%. These results clearly demonstrate the effectiveness of the proposed DSG and MSG modules, which deliver substantial performance gains with only minimal additions in parameters and floating-point operations.

### 3.3. Comparative Experiment

Table 6: Scaling Strategy of YOLOv8, encompassing depth, width, and maximum channel limits.

Models	Depth(%)	Width(%)	Max Channels
N	0.33	0.25	1024
S	0.33	0.50	1024
M	0.67	0.75	768
L	1.00	1.00	512
X	1.00	1.25	512

The YOLOv8-based model is scaled across multiple dimensions—including network depth, channel width, and the maximum channel limit—with specific configurations detailed in Tab.6. As our approach builds upon the YOLOv8 framework, we adopt its established scaling factors (Tab.6) for a fair and direct comparison of performance.

Table 7: Comparison of YOLO-DS and YOLOv8 in terms of AP on MS-COCO val2017.

Models	AP(%)	Params(M)	GFLOPs	Latency(ms/img)
v8-N	37.3	3.2	8.7	1.47
DS-N	38.7 (+1.4)	3.5	9.1	1.51
v8-S	44.9	11.2	28.6	2.66
DS-S	46.6 (+1.7)	12.8	30.0	2.77
v8-M	50.2	25.9	78.9	5.86
DS-M	51.6 (+1.4)	29.6	82.0	6.09
v8-L	52.9	43.7	165.2	9.06
DS-L	54.1 (+1.2)	49.8	170.1	9.31
v8-X	53.9	68.2	257.8	14.37
DS-X	55.0 (+1.1)	77.8	265.5	14.99

Building upon the YOLOv8 scaling strategy, we scale the proposed YOLO-DS model to five standard sizes: N, S, M, L, and X. The detailed configurations are summarized in Tab.6. As shown in the results (Tab.7), the YOLO-DS variants consistently outperform their YOLOv8 counterparts, achieving AP gains of 1.4%, 1.7%, 1.4%, 1.2%, and 1.1%, respectively, across the five scales. Notably, these accuracy improvements are attained within a reasonable increase in inference latency. Overall, the results demonstrate that YOLO-DS delivers a pronounced and scalable performance enhancement over the baseline.

### 3.4. Comparison with SOTA

Tab.8 provides a comprehensive comparison of the proposed YOLO-DS model against contemporary state-of-the-art YOLO detectors across five standardized scales on MS-COCO val2017. The results underscore a key strength of YOLO-DS: it consistently surpasses the widely deployed YOLOv8 baseline across all model scales (N, S, M, L, X), with AP gains ranging from +1.4% to +1.7%. This robust and scale-agnostic improvement directly validates the efficacy of the introduced DSG and MSG modules in enhancing discriminative feature learning within the YOLO architecture.

Table 8: Comparative Evaluation of AP and Inference Latency Across SOTA Object Detectors on MS-COCO val2017. All models use input size 640.

Model	N	S	M	L	X
	Lat./AP	Lat./AP	Lat./AP	Lat./AP	Lat./AP
YOLOv8[12]	1.47/37.3	2.66/44.9	5.86/50.2	9.06/52.9	14.37/53.9
YOLOv9[13]	2.30/38.3	3.54/46.8	6.43/51.4	7.16/53.0	16.77/ <b>55.6</b>
YOLOv10[14]	1.56/38.5	2.66/46.3	5.48/51.1	8.33/53.2	12.20/54.4
YOLO11[15]	1.50/ <b>39.5</b>	2.50/ <b>47.0</b>	4.70/51.5	6.20/53.4	11.30/54.7
YOLO-DS	1.51/38.7	2.77/46.6	6.09/ <b>51.6</b>	9.31/ <b>54.1</b>	14.99/55.0

Notably, YOLO-DS achieves superior AP at medium and large model sizes (M, L), outperforming all other compared models. This demonstrates that our modules are particularly effective when the model has sufficient capacity, excelling in scenarios that demand higher accuracy. For smaller-scale models (N, S), YOLO-DS delivers highly competitive accuracy, closely

approaching the top-performing model while maintaining a nearly identical inference latency. At the extreme X scale, YOLO-DS achieves a strong second-place AP, significantly outperforming YOLOv8 and YOLOv10, and trading a marginal accuracy gap for a considerable latency advantage over the heaviest model.

Overall, YOLO-DS establishes an excellent accuracy-latency Pareto front. Its primary contribution is not merely achieving a singular top score, but delivering reliable and scalable performance enhancements over a strong baseline (YOLOv8) across the entire model family. This makes YOLO-DS a versatile and effective upgrade, offering a favorable trade-off that prioritizes consistent gains in detection accuracy with minimal computational overhead, which is crucial for practical deployment.

#### 4. Conclusion

To address the issue of coupled heterogeneous object features in existing YOLO detectors, this paper proposes YOLO-DS, a fine-grained feature decoupling framework based on a Dual-Statistic Synergy Operator (DSO). By jointly modeling channel-wise mean and peak-to-mean difference, the DSO effectively distinguishes object responses of different scales and backgrounds within a two-dimensional decision space. Building upon this, the designed Dual-Statistic Synergy Gating (DSG) and Multi-Path Segmented Gating (MSG) modules adaptively perform feature gating and selection from the dimensions of feature channels and network depths, respectively. Comprehensive experiments on the MS-COCO dataset demonstrate that YOLO-DS achieves consistent improvements across all five scales (N, S, M, L, X)

of YOLOv8, with AP gains ranging from 1.1% to 1.7%, while incurring only a manageable increase in inference latency. Visualization analysis, ablation studies, and comparative experiments confirm the efficacy of each module, indicating that the proposed framework significantly enhances the model’s ability to discriminate heterogeneous objects at a minimal computational cost. This work provides a reliable and scalable solution for balancing accuracy and efficiency in real-time detection systems.

## 5. Acknowledgments

This work was supported in part by the National Natural Science Foundation of China under Grant No.62472058 and No.62572085, the Natural Science Foundation of Shandong Province under Grant No.ZR2024LZH013, and the State KeyLab of Processors in Institute of Computing Technology under CAS Grant No.CLQ202510.

## References

- [1] J. Redmon, S. Divvala, R. Girshick, A. Farhadi, You only look once: Unified, real-time object detection, in: Proceedings of the IEEE conference on computer vision and pattern recognition, 2016, pp. 779–788.
- [2] J. Redmon, A. Farhadi, Yolo9000: better, faster, stronger, in: Proceedings of the IEEE conference on computer vision and pattern recognition, 2017, pp. 7263–7271.
- [3] J. Redmon, A. Farhadi, Yolov3: An incremental improvement, arXiv preprint arXiv:1804.02767 (2018).

- [4] A. Bochkovskiy, C.-Y. Wang, H.-Y. M. Liao, Yolov4: Optimal speed and accuracy of object detection, arXiv preprint arXiv:2004.10934 (2020).
- [5] C.-Y. Wang, A. Bochkovskiy, H.-Y. M. Liao, Scaled-yolov4: Scaling cross stage partial network, in: Proceedings of the IEEE/cvf conference on computer vision and pattern recognition, 2021, pp. 13029–13038.
- [6] G. Jocher, Ultralytics yolov5 (2020). doi:10.5281/zenodo.3908559  
URL <https://github.com/ultralytics/yolov5>
- [7] X. Long, K. Deng, G. Wang, Y. Zhang, Q. Dang, Y. Gao, H. Shen, J. Ren, S. Han, E. Ding, et al., Pp-yolo: An effective and efficient implementation of object detector, arXiv preprint arXiv:2007.12099 (2020).
- [8] X. Huang, X. Wang, W. Lv, X. Bai, X. Long, K. Deng, Q. Dang, S. Han, Q. Liu, X. Hu, et al., Pp-yolov2: A practical object detector, arXiv preprint arXiv:2104.10419 (2021).
- [9] Q. Chen, Y. Wang, T. Yang, X. Zhang, J. Cheng, J. Sun, You only look one-level feature, in: Proceedings of the IEEE/CVF conference on computer vision and pattern recognition, 2021, pp. 13039–13048.
- [10] Z. Ge, S. Liu, F. Wang, Z. Li, J. Sun, Yolox: Exceeding yolo series in 2021, arXiv preprint arXiv:2107.08430 (2021).
- [11] C.-Y. Wang, A. Bochkovskiy, H.-Y. M. Liao, Yolov7: Trainable bag-of-freebies sets new state-of-the-art for real-time object detectors, arXiv preprint arXiv:2207.02696 (2022).

- [12] G. Jocher, A. Chaurasia, J. Qiu, Ultralytics yolov8 (2023).  
URL <https://github.com/ultralytics/ultralytics>
- [13] C.-Y. Wang, H.-Y. M. Liao, Yolov9: Learning what you want to learn using programmable gradient information (2024).
- [14] L. L. e. a. Ao Wang, Hui Chen, Yolov10: Real-time end-to-end object detection, arXiv preprint arXiv:2405.14458 (2024).
- [15] G. Jocher, J. Qiu, Ultralytics yolo11 (2024).  
URL <https://github.com/ultralytics/ultralytics>
- [16] T.-Y. Lin, P. Goyal, R. Girshick, K. He, P. Dollár, Focal loss for dense object detection, in: Proceedings of the IEEE international conference on computer vision, 2017, pp. 2980–2988.
- [17] M. Tan, R. Pang, Q. V. Le, Efficientdet: Scalable and efficient object detection, in: Proceedings of the IEEE/CVF conference on computer vision and pattern recognition, 2020, pp. 10781–10790.
- [18] S. Liu, D. Huang, Y. Wang, Learning spatial fusion for single-shot object detection, arXiv preprint arXiv:1911.09516 (2019).
- [19] W. Liu, D. Anguelov, D. Erhan, C. Szegedy, S. Reed, C.-Y. Fu, A. C. Berg, Ssd: Single shot multibox detector, in: Computer Vision–ECCV 2016: 14th European Conference, Amsterdam, The Netherlands, October 11–14, 2016, Proceedings, Part I 14, Springer, 2016, pp. 21–37.
- [20] R. Qian, X. Lai, X. Li, 3d object detection for autonomous driving: A survey, Pattern Recognition 130 (2022) 108796.

- [21] G. Antipov, M. Baccouche, S.-A. Berrani, J.-L. Dugelay, Effective training of convolutional neural networks for face-based gender and age prediction, *Pattern Recognition* 72 (2017) 15–26.
- [22] H. Guan, P.-T. Yap, A. Bozoki, M. Liu, Federated learning for medical image analysis: A survey, *Pattern Recognition* (2024) 110424.
- [23] C. Wang, W. Zhu, B.-B. Gao, Z. Gan, J. Zhang, Z. Gu, S. Qian, M. Chen, L. Ma, Real-iad: A real-world multi-view dataset for benchmarking versatile industrial anomaly detection, in: *Proceedings of the IEEE/CVF Conference on Computer Vision and Pattern Recognition*, 2024, pp. 22883–22892.
- [24] J. Hu, L. Shen, G. Sun, Squeeze-and-excitation networks, in: *Proceedings of the IEEE conference on computer vision and pattern recognition*, 2018, pp. 7132–7141.
- [25] S. Woo, J. Park, J.-Y. Lee, I. S. Kweon, Cbam: Convolutional block attention module, in: *Proceedings of the European conference on computer vision (ECCV)*, 2018, pp. 3–19.
- [26] A. Dosovitskiy, L. Beyer, A. Kolesnikov, D. Weissenborn, X. Zhai, T. Unterthiner, M. Dehghani, M. Minderer, G. Heigold, S. Gelly, et al., An image is worth 16x16 words: Transformers for image recognition at scale, *arXiv preprint arXiv:2010.11929* (2020).
- [27] O. M. Shir, M. Preuss, B. Naujoks, M. Emmerich, Enhancing decision space diversity in evolutionary multiobjective algorithms, in: *In-*

ternational Conference on Evolutionary Multi-Criterion Optimization, Springer, 2009, pp. 95–109.

- [28] T.-Y. Lin, M. Maire, S. Belongie, J. Hays, P. Perona, D. Ramanan, P. Dollár, C. L. Zitnick, Microsoft coco: Common objects in context, in: Computer Vision–ECCV 2014: 13th European Conference, Zurich, Switzerland, September 6–12, 2014, Proceedings, Part V 13, Springer, 2014, pp. 740–755.
- [29] K. He, X. Zhang, S. Ren, J. Sun, Deep residual learning for image recognition, in: Proceedings of the IEEE conference on computer vision and pattern recognition, 2016, pp. 770–778.
- [30] D. Garcia-Gasulla, F. Parés, A. Vilalta, J. Moreno, E. Ayguadé, J. Labarta, U. Cortés, T. Suzumura, On the behavior of convolutional nets for feature extraction, *Journal of Artificial Intelligence Research* 61 (2018) 563–592.
- [31] J. Yosinski, J. Clune, Y. Bengio, H. Lipson, How transferable are features in deep neural networks?, *Advances in neural information processing systems* 27 (2014).
- [32] N. Tishby, F. C. Pereira, W. Bialek, The information bottleneck method, *arXiv preprint physics/0004057* (2000).
- [33] M. B. Muhammad, M. Yeasin, Eigen-cam: Class activation map using principal components, in: 2020 international joint conference on neural networks (IJCNN), IEEE, 2020, pp. 1–7.